Supplementary information of "Realization of fast all-microwave CZ gates with a tunable coupler"

Shaowei Li,[1,2,3] Daojin Fan,[1,2,3] Ming Gong,[1,2,3] Yangsen Ye,[1,2,3] Xiawei Chen,[1,2,3] Yulin Wu,[1,2,3] Huijie Guan,[1,2,3] Hui Deng,[1,2,3] Hao Rong,[1,2,3] He-Liang Huang,[1,2,3] Chen Zha,[1,2,3] Kai Yan,[1,2,3] Shaojun Guo,[1,2,3] Haoran Qian,[1,2,3] Haibin Zhang,[1,2,3] Fusheng Chen,[1,2,3] Qingling Zhu,[1,2,3] Youwei Zhao,[1,2,3] Shiyu Wang,[1,2,3] Chong Ying,[1,2,3] Sirui Cao,[1,2,3] Jiale Yu,[1,2,3] Futian Liang,[1,2,3] Yu Xu,[1,2,3] Jin Lin,[1,2,3] Cheng Guo,[1,2,3] Lihua Sun,[1,2,3] Na Li,[1,2,3] Lianchen Han,[1,2,3] Cheng-Zhi Peng,[1,2,3] Xiaobo Zhu,[1,2,3,*] and Jian-Wei Pan[1,2,3]

[1]*Department of Modern Physics, University of Science and Technology of China, Hefei 230026, China*

[2]*Shanghai Branch, CAS Center for Excellence in Quantum Information and Quantum Physics, University of Science and Technology of China, Shanghai 201315, China*

[3]*Shanghai Research Center for Quantum Sciences, Shanghai 201315, China*

(Dated: January 30, 2022)

---

* xbzhu16@ustc.edu.cn

I. NUMERICAL SIMULATION OF CZ GATE

We designed three different couplers and compared the quality of different designs according to the CZ error achieved under different qubit detune frequency $\Delta = \omega_{10} - \omega_{01}$. We first set $g = 0$ for three types of the coupler, labeled as Con. 1, Con. 2, and Con. 3. We set different g for idle working points to find the effect of idle point setting, labeled as Con. 3, Con. 4, and Con. 5. Also, we test the influence of envelopes of the microwave by comparing two types of envelopes labeled as Con. 3, and Con. 6. Fig.S1 shows 6 condition for numerical simulation. Fig.S2 shows the different CZ error results between coupler design 1 and coupler design 3. Fig.S3 shows the different CZ error results between coupler design 2 and coupler design 3. Fig.S4 shows the results of different coupling strength setting for idle points. Fig.S5 shows the results of different initial envelope settings for idle points.

For each $\Delta/2\pi$ in Fig. 4(d) in main text, we set the initial ratio of $\vec{\lambda}$ as $\lambda_1 : \lambda_2 : \lambda_3 : \lambda_4 = -0.0760 : 1.0000 : 0.4222 : -0.1636$, and chose static frequency difference between $|11\rangle$ and $|20\rangle$ as the initial microwave frequency. Also, the averaging microwave amplitude $\bar{A}(t)$ was set to be 0.4, 0.045 or 0.05. Then we used the Nelder Mead algorithm to optimize the fidelity of the CZ gate. Fig.S6 and Fig.S7 show the numerical optimization and time domain evolution at $\Delta/2\pi = 0.11724$ GHz, where no unwanted interaction is activated and CZ gate with 99.99972% fidelity is achieved. Fig.S8 and Fig.S9 show the numerical optimization and time domain evolution at $\Delta/2\pi = 0.09248$ GHz, where no unwanted interaction is activated and CZ gate with 99.99960% fidelity is achieved. Fig.S10 and Fig.S11 show the numerical optimization and time domain evolution at $\Delta/2\pi = 0.10486$ GHz, where the interaction between $|01\rangle$ and $|01\rangle$ is activated and the optimized CZ fidelity is 99.75%. Fig.S12 and Fig.S13 show the numerical optimization and time domain evolution at $\Delta/2\pi = 0.07391$ GHz, where the interaction between $|11\rangle$ and $|02\rangle$ activated and the optimized CZ fidelity is 99.39%.

II. EXPERIMENT OF CZ GATE

The definition of cross entropy benchmarking (XEB) is as below,

$$\alpha = \frac{\overline{\sum_q p_m(q)(Dp_s(q) - 1)}}{D\sum_q \overline{p_s(q)^2} - 1} \tag{S1}$$

with α as the sequence fidelity, $D = 2^N$, N is the number of qubits, q is the sampled qubit state bitstrings (for single-qubit XEB, q is 0 or 1), $p_s(q)$ is the ideal probability of q, and $p_m(q)$ is the measured probability of q. The over lines in Eq. S1 refer to the average of the random circuits in each cycle. Meanwhile, we use the speckle purity benchmarking (SPB) to measure the effect of decoherence error. Here,

$$\sqrt{P} = \sqrt{Var(p_m)\frac{D^2(D+1)}{D-1}}. \tag{S2}$$

and $Var(P_m)$ the variance of the experimental probabilities extracted from the XEB experiment.

Due to the readout error, the start points (m = 0) of α are not at 1 in Fig.4(c) and (d). The setting of readout pulse in our experiment was different for $|0\rangle$, $|1\rangle$ measurement and for $|0\rangle$, $|1\rangle$, $|2\rangle$ measurement. For $|0\rangle$, $|1\rangle$ measurement, the matrixes of readout fidelity are labeled as below,

$$\begin{pmatrix} F_{00} & F_{01} \\ F_{10} & F_{11} \end{pmatrix}_{Q1} = \begin{pmatrix} 0.9551 & 0.0449 \\ 0.1581 & 0.8419 \end{pmatrix} \tag{S3}$$

and

$$\begin{pmatrix} F_{00} & F_{01} \\ F_{10} & F_{11} \end{pmatrix}_{Q2} = \begin{pmatrix} 0.9475 & 0.0525 \\ 0.1517 & 0.8483 \end{pmatrix}. \tag{S4}$$

For $|0\rangle$, $|1\rangle$, $|2\rangle$ measurement, the matrixes of readout fidelity are labeled as below,

$$\begin{pmatrix} F_{00} & F_{01} & F_{02} \\ F_{10} & F_{11} & F_{12} \\ F_{20} & F_{21} & F_{22} \end{pmatrix}_{Q1} = \begin{pmatrix} 0.9050 & 0.0632 & 0.0318 \\ 0.1633 & 0.7779 & 0.0588 \\ 0.1383 & 0.2005 & 0.6612 \end{pmatrix} \tag{S5}$$

and

$$\begin{pmatrix} F_{00} & F_{01} & F_{02} \\ F_{10} & F_{11} & F_{12} \\ F_{20} & F_{21} & F_{22} \end{pmatrix}_{Q2} = \begin{pmatrix} 0.8767 & 0.0534 & 0.0699 \\ 0.1887 & 0.7399 & 0.0714 \\ 0.1645 & 0.1784 & 0.6571 \end{pmatrix}. \tag{S6}$$

Here F_{ij} represents the probability of measuring $|j\rangle$ when we prepared the initial state of $|i\rangle$. In experiment, we used the product of each matrix of single-qubit readout fidelity as the matrix of multi-qubit readout fidelity. In Fig.4(c) and (d), the α and $\sqrt{P}$ are calculated by the raw probability of $|0\rangle$, $|1\rangle$ measurement, and the $leak$ is the probability corrected according to the matrix of multi-qubit readout fidelity of $|0\rangle$, $|1\rangle$, $|2\rangle$ measurement. Here, $leak = P_{|02\rangle} + P_{|12\rangle} + P_{|20\rangle} + P_{|21\rangle} + P_{|22\rangle}$.
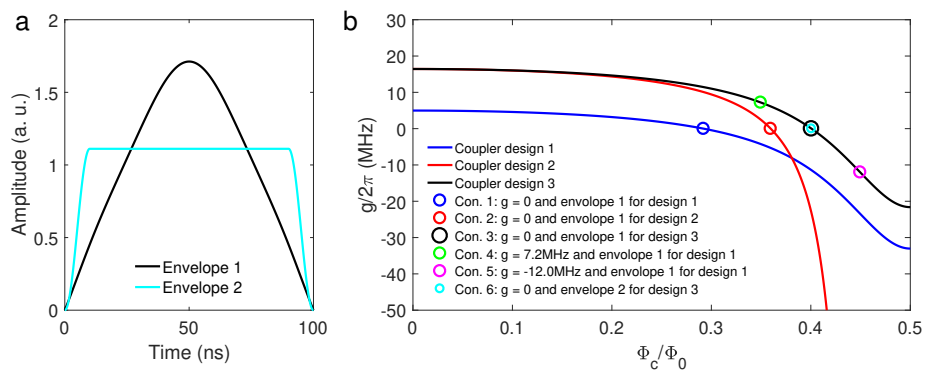
FIG. S1. Different coupler designs, idle points and initial envelopes for condition 1 (con. 1) to condition 6.
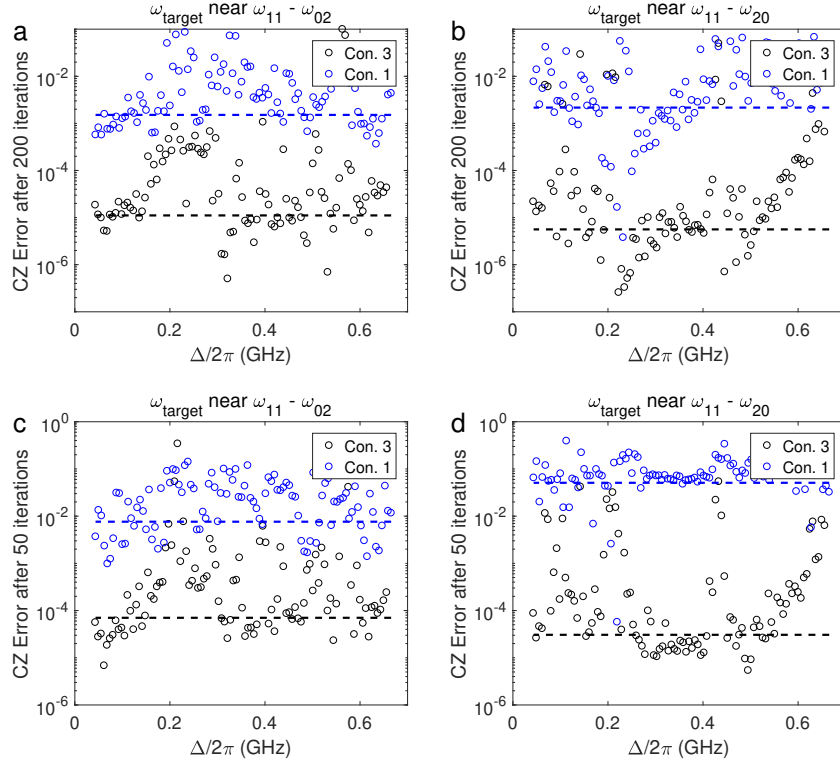
FIG. S2. Results of Con. 3 and Con. 1 of CZ optimization. (a) CZ error under the con. 1 and con. 3 for selecting ω_{target} near $\omega_{11} - \omega_{02}$. The circles are CZ errors under con. 3 and con. 1 after 200 iteration of Nelder Mead algorithm for different Δ. For some of Δ, the unnecessary resonance interactions will increase the gate error, see Fig. 2 (d) in main text. We selected the best 50 from the results of all 100 different Δ to calculate the average error rate, as shown by the dash line. (b) CZ error under the con. 1 and con. 3 for selecting ω_{target} near $\omega_{11} - \omega_{20}$ after 200 iteration. (c) CZ error under the con. 1 and con. 3 for selecting ω_{target} near $\omega_{11} - \omega_{02}$ after 50 iteration. (d) CZ error under the con. 1 and con. 3 for selecting ω_{target} near $\omega_{11} - \omega_{20}$ after 50 iteration.
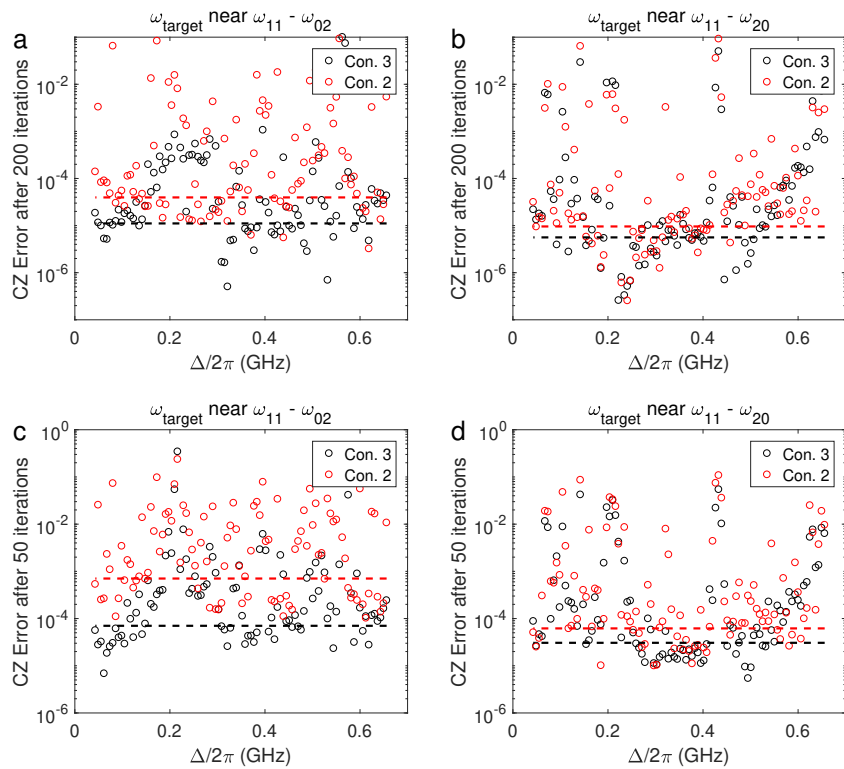
FIG. S3. Results of Con. 3 and Con. 2 of CZ optimization.
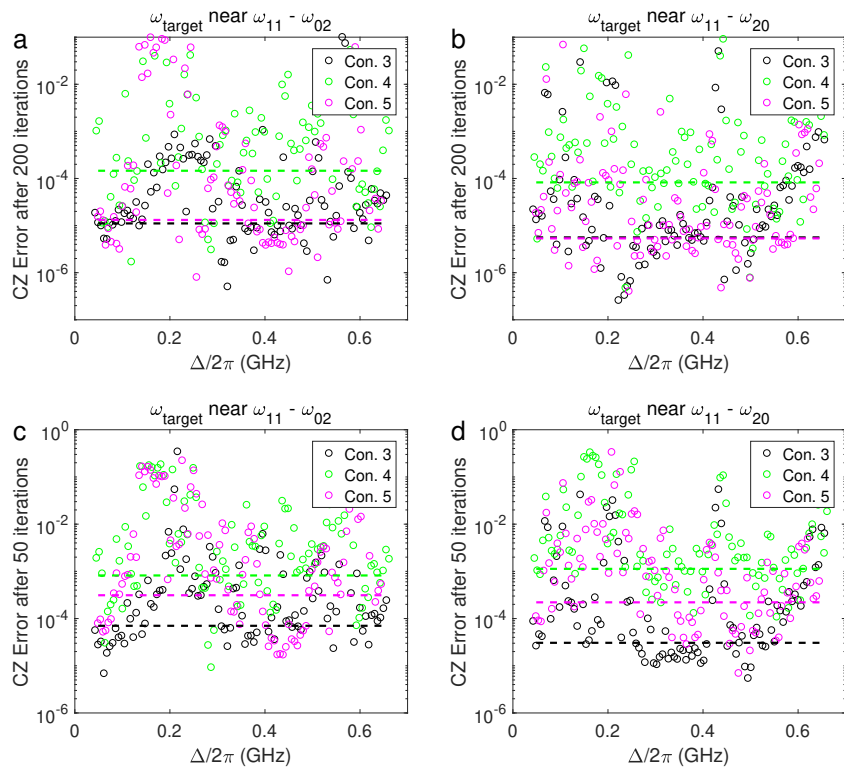
FIG. S4. Results of Con. 3, Con. 4 and Con. 5 of CZ optimization.
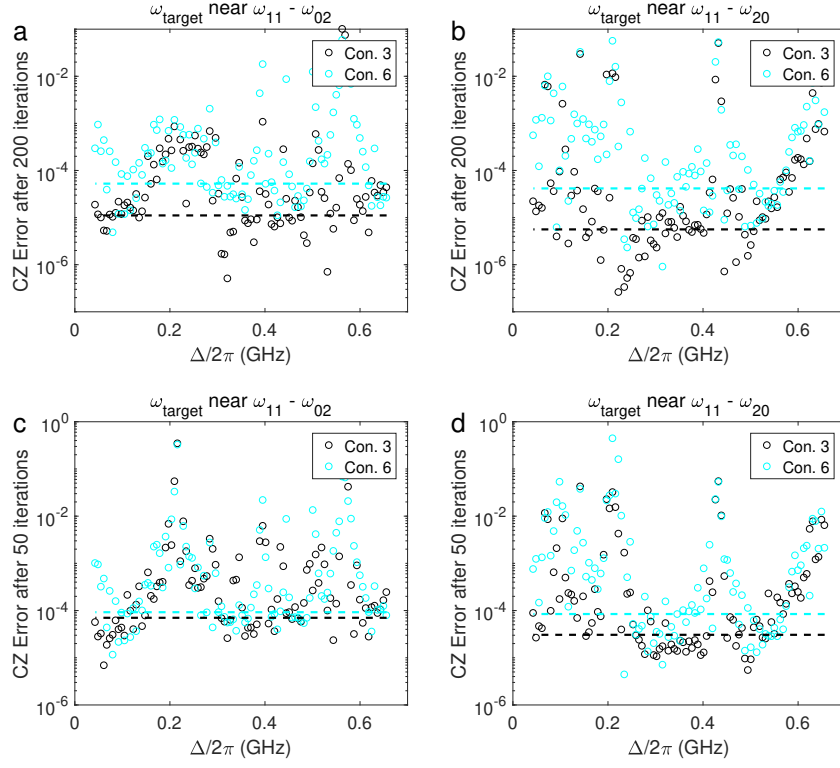
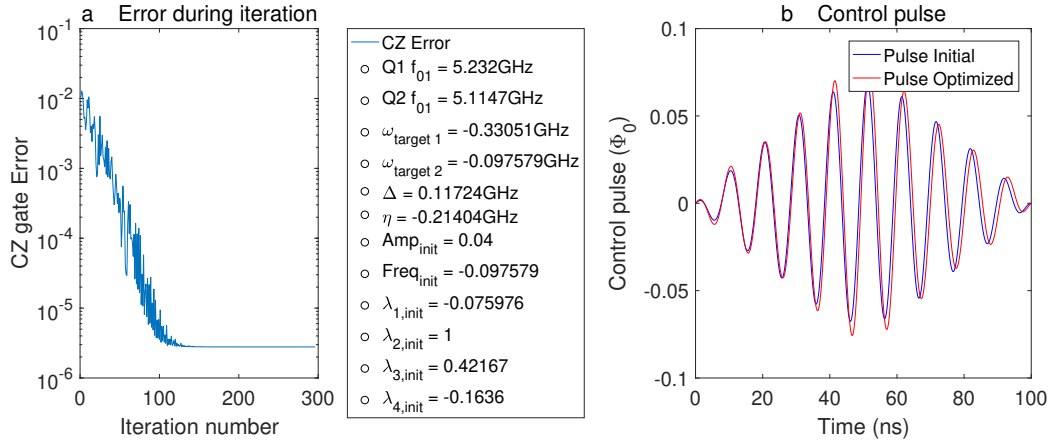FIG. S5. Results of Con. 3 and Con. 6 of CZ optimization.

FIG. S6. Numerical optimization at $\Delta/2\pi = 0.11724$ GHz in Fig. 2(d) in main text. (a) shows the qubits work point, initial value of CZ pulse and CZ gate error during iteration. (b) shows the control pulse before and after optimization.
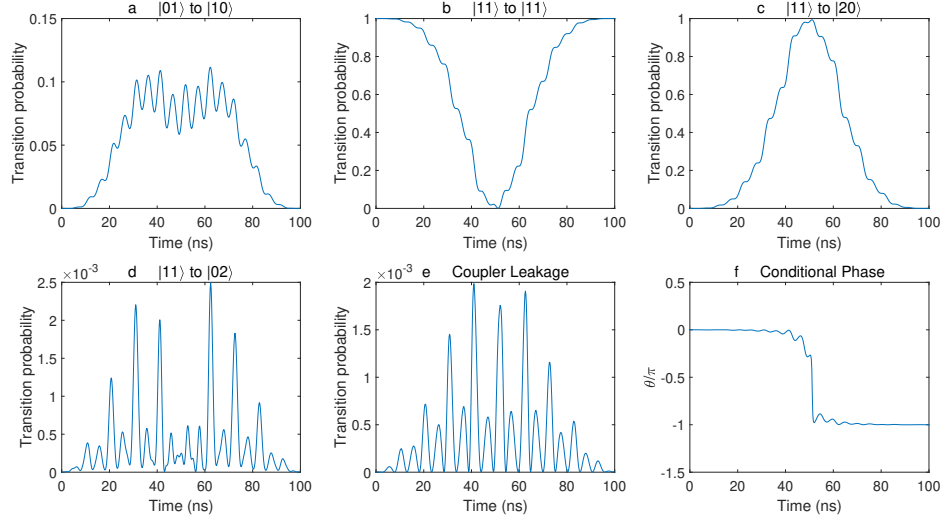
FIG. S7. Time domain quantum evolution for optimized CZ pulse at $\Delta/2\pi = 0.11724$ GHz (data obtained by numerical simulation method). The quantum state in this figure is the energy eigenstate of the static Hamiltonian. (a) (d) show the transtion probability between different quantum states. (e) shows the probability of leakage into the excited state of the coupler. (f) shows the conditional phase during the evolution.
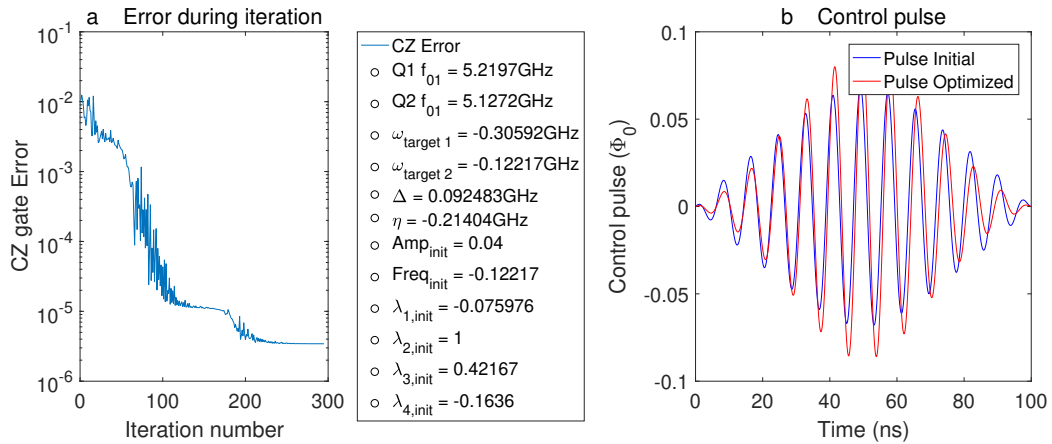

FIG. S8. Numerical optimization at $\Delta/2\pi = 0.09248$ GHz in Fig. 2(d) in main text.
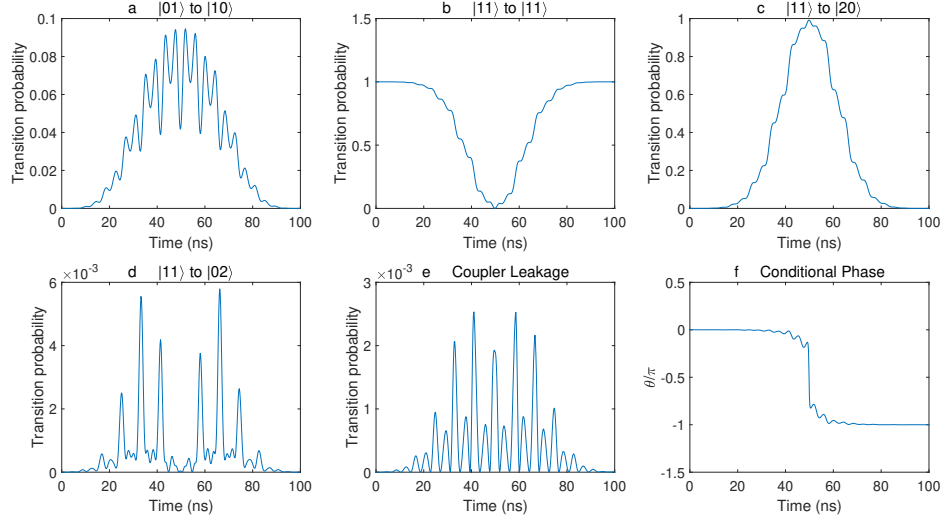
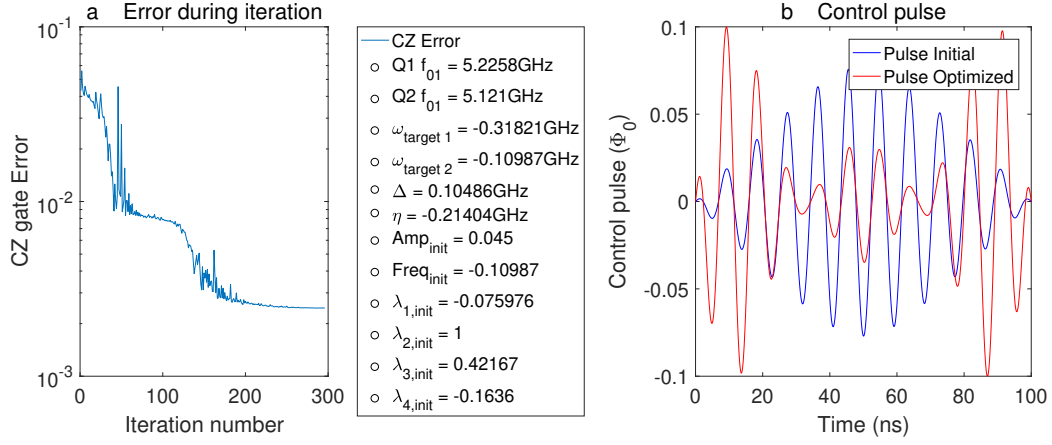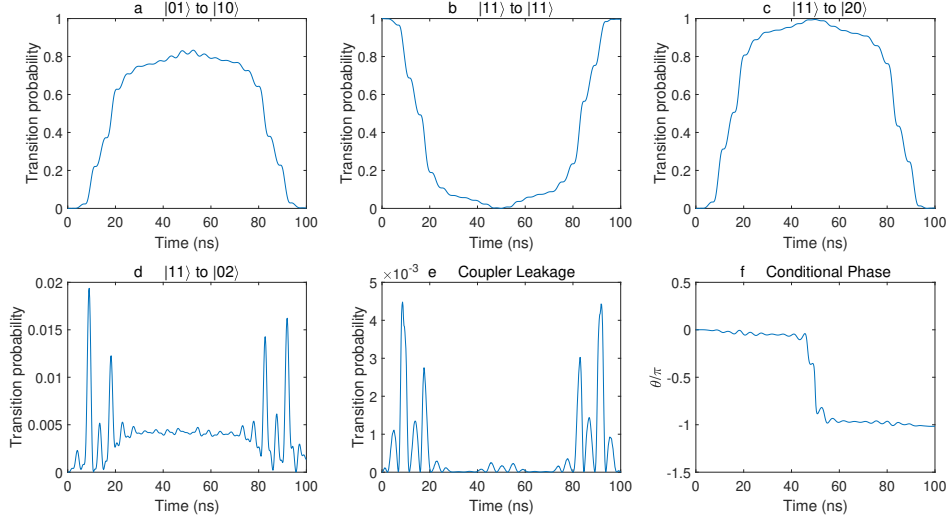FIG. S9. Time domain quantum evolution for optimized CZ pulse at $\Delta/2\pi = 0.09248$ GHz.

FIG. S10. Numerical optimization at $\Delta/2\pi = 0.10486$ GHz in Fig. 2(d) in main text. For this Δ, the interaction between $|01\rangle$ and $|10\rangle$ is activated.

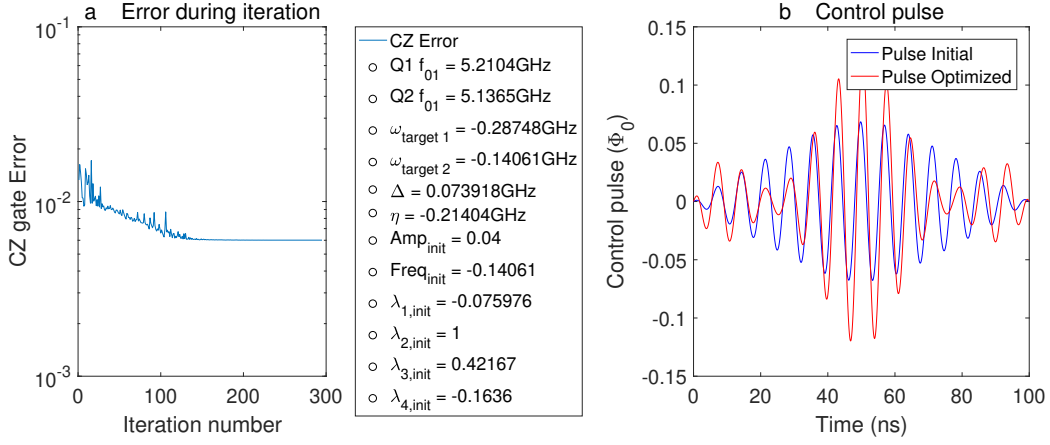FIG. S11. Time domain quantum evolution for optimized CZ pulse at $\Delta/2\pi = 0.10486$ GHz.

FIG. S12. Numerical optimization at $\Delta/2\pi = 0.07392$ GHz in Fig. 2(d) in main text. For this Δ, the interaction between $|11\rangle$ and $|02\rangle$ is activated.
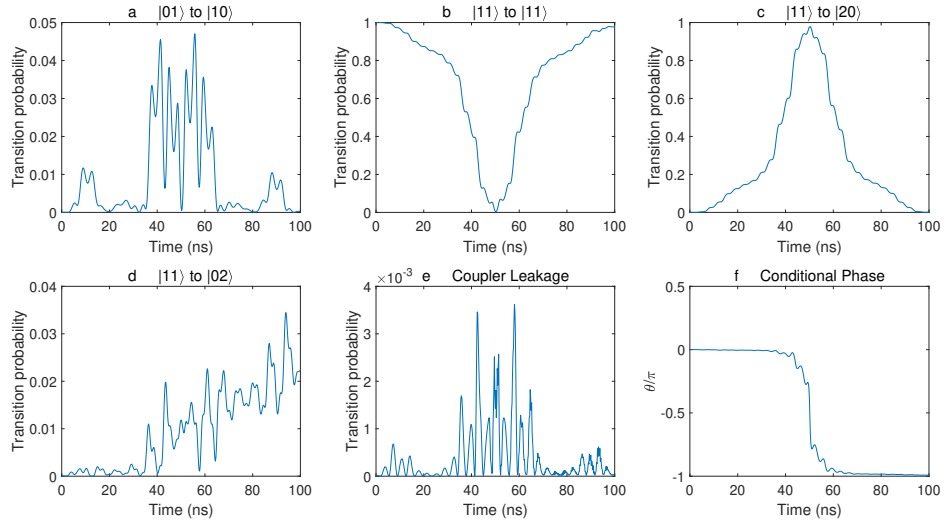
FIG. S13. Time domain quantum evolution for optimized CZ pulse at $\Delta/2\pi = 0.07392$ GHz.